

In Operando Strain Measurement of Bicontinuous Silicon-Coated Nickel Inverse Opal Anodes for Li-Ion Batteries

Matthew P. B. Glazer, Jiung Cho, Jonathan Almer, John Okasinski, Paul V. Braun, and David C. Dunand*

Elastic strains are measured in operando in a nanostructured silicon-coated nickel inverse opal scaffold anode, using X-ray diffraction to study the Si (de)lithiation-induced Ni strains. The volume expansion upon lithiation of the Si in the anode is constrained by the surrounding Ni scaffold, causing mismatch stresses and strains in the Si and Ni phases during cycling. The Ni strains are measured in operando during (dis)charge cycles, using diffraction peak position and peak broadness to describe the distribution of strain in the Ni. During lithiation, compressive strains in the Ni first increase linearly with charge, after which a gradually decreasing strain rate is observed as the maximum lithiation state is approached; upon delithiation a similar process occurs. In-plane average compressive strains on the order of $990 \pm 40 \mu\epsilon$ are measured in the Ni scaffold during lithiation, corresponding to compressive stresses of 215 ± 9 MPa. The decreasing strain rates and decreasing maximum and recovered strains suggest that plasticity in Ni and/or Si, as well as delamination between Ni and Si, may occur during cycling. Rate sensitivity in capacity is correlated with strain and a maximum Ni compressive stress of 230 ± 40 MPa is measured at the maximum state of lithiation.

1. Introduction

Lithium ion batteries (LIBs) represent an efficient and modular energy storage solution for a wide variety of portable applications but will require substantially higher energy densities and shorter charging times to meet emerging demand for electric vehicles

M. P. B. Glazer, Prof. D. C. Dunand
Department of Materials Science and Engineering
Northwestern University
2220 Campus Drive, Attention Room 2036
Evanston, IL 60208, USA
E-mail: dunand@northwestern.edu

Dr. J. Cho, Prof. P. V. Braun
Department of Materials Science and Engineering
University of Illinois at Urbana-Champaign
Champaign, IL 61801, USA

Dr. J. Cho
Gangneung Center
Korea Basic Science Institute
Gangneung 210-702, South Korea

Dr. J. Almer, Dr. J. Okasinski
X-ray Science Division
Argonne National Laboratory
Argonne, IL 60439, USA

DOI: 10.1002/aenm.201500466



and other applications.^[1-4] Alloying anode materials, such as silicon, are very promising because of their high gravimetric energy densities (up to 3580 mAh g⁻¹ for Si)^[5] as compared to graphite (up to 372 mAh g⁻¹ for C),^[6] and the high abundance of Si, but silicon suffers from very high volume changes (>300%) during lithiation.^[6] These volume changes can generate very large stresses, which lead to the delamination, cracking, and pulverization of Si based anodes, ultimately causing rapid capacity fading. The fundamental nature of this volume change process associated with alloying has been well explored in the literature by employing ex situ scanning electron microscopy (SEM), transmission electron microscopy (TEM), and atomic force microscopy (AFM), as well as atomistic simulations and theoretical calculations.^[6-9] Some in operando studies^[10-15] have explored this lithiation-induced expansion during cycling for simple anode geometries, limited in part

by the amorphous nature of the alloying mechanism and the difficulty of designing in operando experiments. Only three studies have employed galvanostatic cycling methods, which may be more representative of future applications.^[11-13]

To investigate lithiation strains in Si during cycling, some in situ and in operando studies have been performed for simple geometries.^[8,10,11,13-18] These studies have employed AFM, TEM and optical laser measurement techniques to measure strains, with AFM and TEM techniques also able to characterize morphology and identify fracture. AFM and TEM studies are able to identify plasticity, cracking and failure occurring in operando and can estimate critical stresses and sizes for nanowires, nanopillars, and other shapes.^[10,14-16] These in situ/operando studies are effective for describing average lithiation stresses and strains that exist on surfaces or anodes with simple geometries but cannot directly measure the spatial distributions of strain that may exist in more complex geometries and structures as well as at buried interfaces, especially for technologically or commercially relevant anode geometries.

X-ray diffraction (XRD) based strain measurements are able to directly measure elastic strain distributions in arbitrary geometries, bulk materials, and buried interfaces between different phases or materials in a sample that might not be easily accessible in situ/operando otherwise. XRD has been used effectively to describe average strains, strain distributions,

and multiphase strain partitioning in a variety of materials systems.^[19–27] Through changes in diffraction peak position, width, intensity, and shape, one can effectively characterize elasto-plastic deformation and load transfer mechanisms across multiple phases as well as residual stresses with a high degree of precision and accuracy.^[22–27] While some researchers have used XRD to characterize the transition between crystalline and amorphous Si during the first cycle or at high degrees of lithiation,^[28–32] none have characterized strains in nanostructured anodes employing amorphous Si.

Here we demonstrate, for the first time, that synchrotron-based X-ray diffraction can characterize strains in a Li-alloying anode in operando during charging/discharging cycles. Specifically, we measure the magnitude and distribution of strains in a novel anode consisting of a nickel-inverse opal scaffold coated by nanostructured, amorphous silicon (a-Si). Mismatch strains between the Ni scaffold and Si active layer due to the volume change associated with the (de)lithiation of Si during (dis)charging are measured, using both Ni average lattice crystallographic strain and crystallographic strain broadening, at even time intervals during galvanostatic cycling at different cycling rates. The results are discussed in terms of elasto-plastic deformation and possible a-Si delamination from the scaffold.

2. Results

2.1. In-Plane Average Lattice Strains

Examining the lattice strain measured over various orientations, a residual, nonuniform strain distribution was observed

in the Ni (200) and (220) diffraction rings before the first lithiation. Figure S1 (Supporting Information) shows the measured lattice spacing for Ni (200) and Ni (220) during L1 as a function of η . Although a nonuniform distribution of strain is initially present in the Ni scaffold, the average in-plane strain value changes significantly with increasing lithiation, while the distribution of individual azimuthal sections' strain values around the average only changes slightly during lithiation. Therefore examining the azimuthally averaged in-plane strain response in the Ni scaffold separates many of the changes observed during lithiation from possible residual processing strains, which may be responsible for the azimuthal variation in strain. Additional lattice strain analysis other than what was described in the Experimental Section is available in Figures S2–S4 (Supporting Information).

Figure 1 shows the in-plane average crystallographic strain present in the Ni scaffold during lithiation of the Si anode for the Ni (200), (220), and (311) rings during the first cycling series. The Ni (111) ring was also measured but is not included due to fitting errors associated with the overlap of the Al (200) (Figure S5, Supporting Information). During the first half of L1, all three of the Ni rings show roughly linear increases in compressive strain over time as the degree of lithiation increases, indicating that mismatch strains associated with lithiation in the Si are present in the Ni scaffold, where Ni strains are measurable by X-ray diffraction. The differences in the slope of the strain curves and the magnitude of the compressive strains observed between Ni (200), Ni (220), and Ni (311) correlate linearly with their differences in stiffness (approximately 137 GPa for (200), 233 GPa for (220), and

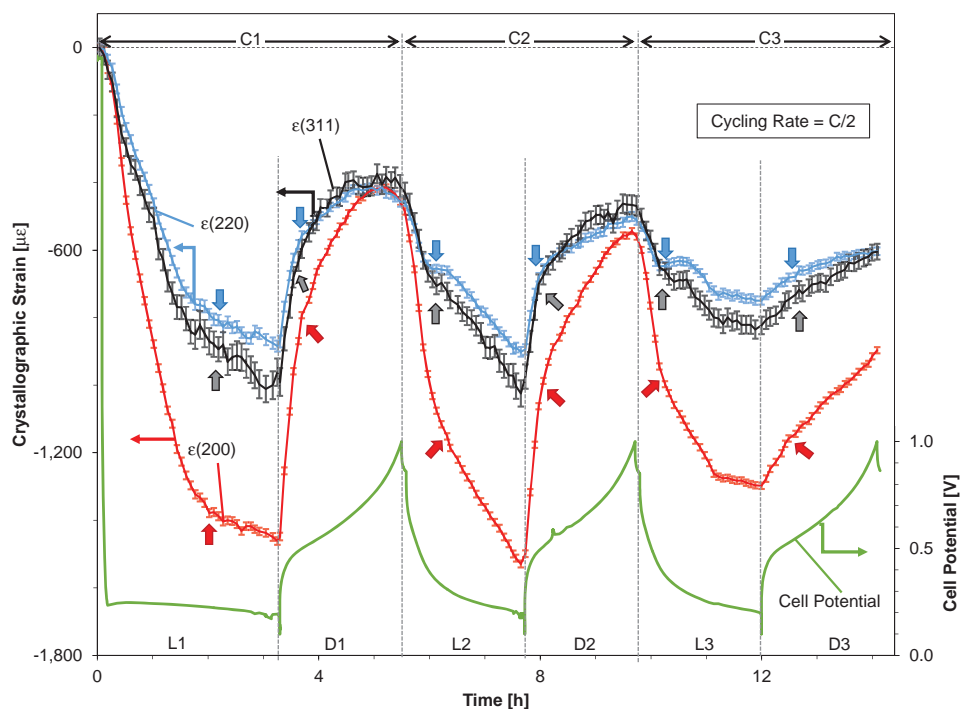


Figure 1. Time dependence of in-plane average crystallographic strains as measured in Ni (200), (220), and (311) (left axis) and electrochemical cell potential (right axis vs Li/Li⁺) (Series 1, consisting of cycles C1, C2, and C3, where the lithiation and delithiation steps in C1 are denoted L1 and D1, respectively, and so on for C2 and C3). The solid arrows in C1, C2, and C3 indicate the location of the change in strain rate from a linear strain during each (de)lithiation step and the error bars indicate the error estimated for each diffraction ring based on the uncertainty in pixel fitting.

217 GPa for (311)).^[33] The linear increases in strain over time indicate clearly that the Ni scaffold deforms elastically proportional to the degree of lithiation present, and thus the amount of lithiation-induced expansion in the Si active material. In this elastic region, the average in-plane strains measured in the Ni follow Hooke's law, where a linear increase in the lithiation and expansion of the a-Si induces a directly proportional increase in the mismatch at the Si–Ni interface and thus the stresses and elastic strains measured in the Ni scaffold. Strain and cell potential are correlated to the degree of lithiation present in the anode, where the relation between cell potential and capacity for the first cycling series is plotted in Figure S6 (Supporting Information). As lithiation progresses, in the second half of L1, the slope of the strain curves decreases to a shallower slope (the solid arrows in Figure 1), which may indicate yield and plastic deformation of the Ni scaffold, with slower increase in elastic strain. Another hypothesis for the reduction in the slope of the strain curves is that a reduction in mismatch stresses with the Ni scaffold occurs due to delamination between the Si layer and the Ni scaffold, as was also observed in ref. [34]. When an electrically connected segment of Si is no longer constrained by the scaffold, (de)lithiation of that Si segment does not induce strain in the Ni scaffold. At the maximum degree of lithiation in L1, a compressive strain of $990 \pm 40 \mu\epsilon$ was observed in the Ni (311) diffraction ring, corresponding to a crystallographic peak compressive stress of 215 ± 9 MPa. Table 1 summarizes selected maxima and minima in stress and strain for the Ni (311) diffraction ring as well as the strain broadening coefficient (discussed later). Additional strain measurements and stress calculations for the Ni (200) and (220) diffraction rings are included in Table S1 (Supporting Information).

Upon the subsequent first delithiation (D1), a rapid recovery of strain occurs, though strain is not fully recovered from the prelithiation state. Measured compressive strains first rapidly, linearly decrease, followed by a monotonous flattening in the slope of the strain to near zero at the minimum degree of lithiation. The flattening of the slope of the strain at this point could

Table 1. Maximum and minimum compressive strain and stress measurements in the Ni (311) diffraction ring and corresponding strain broadening coefficient fits as calculated for the Ni (111), (200), and (220). The error in the in-plane average strains represents the error estimated for the Ni (311) diffraction ring based on the uncertainty in pixel fitting and the error for the strain broadening coefficient is approximated as the norm of the residuals of fitting for each diffraction pattern.

Cycle step	Ni (311) in-plane average strain [$\mu\epsilon$]	Ni (311) crystallographic stress [MPa]	Ni strain broadening coefficient [%]
L1 minimum	0 ± 30	0 ± 7	0.06 ± 0.03
L1 maximum	990 ± 40	215 ± 9	0.54 ± 0.05
D1 minimum	410 ± 30	89 ± 7	0.27 ± 0.03
L2 maximum	1020 ± 40	221 ± 9	0.42 ± 0.04
D2 minimum	460 ± 30	100 ± 7	0.23 ± 0.02
L3 maximum	840 ± 30	182 ± 7	0.20 ± 0.03
D3 minimum	600 ± 20	130 ± 4	0.01 ± 0.01
L7 maximum	1100 ± 200	230 ± 40	0.71 ± 0.04
L9 maximum	890 ± 80	190 ± 20	0.38 ± 0.03

be due to the effects of the node and strut geometry of the scaffold on the lithiation rate of the coating or to reverse plasticity in the Si or Ni phases. The compressive strain measured in the Ni (311) diffraction ring at the minimum degree of lithiation was $410 \pm 30 \mu\epsilon$, corresponding to a residual compressive stress state of 89 ± 7 MPa. Additionally, in C2 and C3, (de)lithiation follows similar strain behaviors to that shown in C1, though the slope of the strain curves and the maximum compressive strain during lithiation and delithiation decrease from cycle to cycle while the amount of strain recovered at the minimum degree of lithiation also decreases from cycle to cycle. Changes in strain recovery, maximum compressive strain, and the slope of the strain curves all indicate that inelastic processes are occurring in the anode during cycling, including yielding in the Ni scaffold and/or Si active layer, as well as damage at the interface between Ni and Si.

Similar changes to the strains present in the measured Ni peaks in the first series can also be observed in the second experimental series for cycles C6–C9, as shown in Figure 2. The crystallographic strain measured here is indexed to the prelithiation Ni peak positions and some inelastic strain appears to have accumulated during the cycling between the first and second in operando cycling series. During the low voltage lithiation in L7, compressive strain initially increases linearly with time, again indicating elastic deformation. However, as lithiation progresses further, the change in strain measured in the Ni scaffold with increasing lithiation decreases until a plateau region is reached, especially below a cell voltage of 0.100 V (marked by the dotted vertical line in Figure 2). The relation between cell potential and capacity for this experimental series is shown in Figure S7 (Supporting Information). This region (curly bracket in Figure 2) could indicate plastic flow in the Si active layer or Ni scaffold, or damage at the interface between Si and Ni. At the maximum degree of lithiation during this cycle, the Ni scaffold experiences a compressive strain of $1100 \pm 200 \mu\epsilon$ on the Ni (311) diffraction ring, corresponding to a crystallographic compressive stress of 230 ± 40 MPa.

In examining the higher cycling rate cycles C8, C9 and the second half of C7 (D7) in Figure 2, the strain evolution appears to be significantly different in comparison to the strain at high degrees of lithiation (L7, after vertical dotted line at 20 h) as well as the lower cycling rate in C1, C2, and C3 (Figure 1). At the beginning of delithiation in C7, C8, and C9, the strain in the Ni decreases linearly with time, again indicating elastic behavior, followed by an abrupt change to a region with a much shallower decrease in strain over time. This shift could indicate a change in the delithiation mechanism present or a change in the strain gradient present in the active material. While the strain recovered on delithiation between cycles decreases slightly, the maximum compressive strain decreases significantly between cycles, from $1100 \pm 200 \mu\epsilon$ at the beginning of D7, to $890 \pm 80 \mu\epsilon$ at the beginning of D9 on the Ni (311) diffraction ring (see Table 1 and Table S1, Supporting Information, for additional strain data). The decrease in maximum compressive strain indicates rate sensitivity in both capacity and strain and could also indicate that the Si active layer does not have sufficient time to fully delithiate during the delithiation steps, especially given the higher over-potential associated with the higher cycling rate.

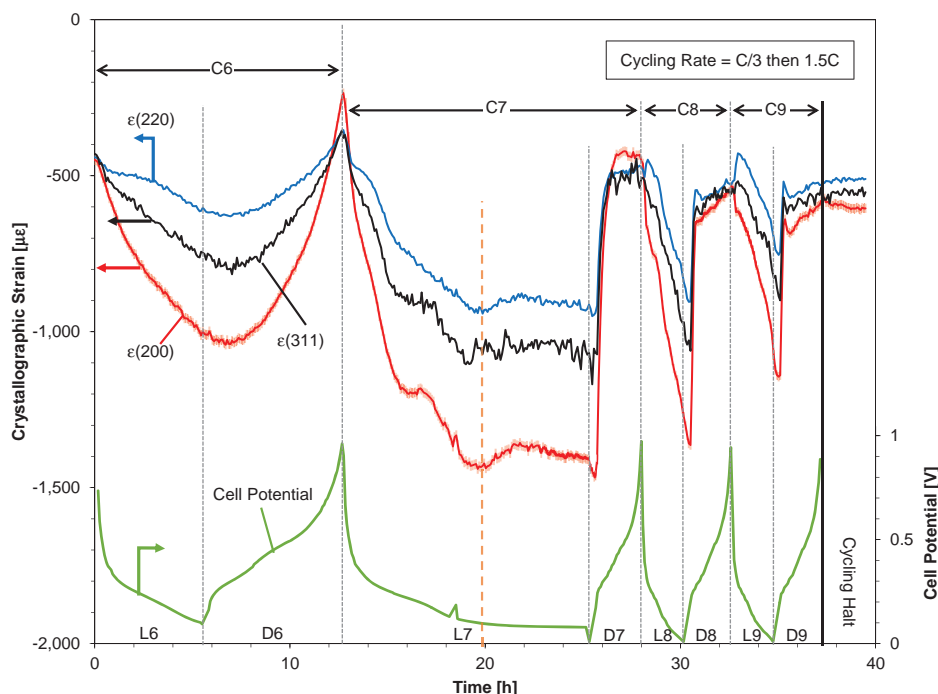


Figure 2. Time dependence of in-plane average crystallographic strain as measured in Ni (200), (220), and (311) and electrochemical cell potential (right axis vs Li/Li⁺) (Series 2 consisting of cycles C6, C7, C8, and C9, where the lithiation and delithiation steps in C6 are denoted L6 and D6, respectively, and so on for C7, C8, and C9). Lithiation at a potential < 100 mV starts at ~20 h (vertical orange dotted line). The error bars shown for (200) strains are representative of the error for (220) and (311) strains and indicate the error estimated based on the uncertainty in pixel fitting.

2.2. Lattice Strain Broadening Coefficient Measurements

In addition to lattice strain measurements, **Figures 3** and **4** show the results of strain broadening coefficient analysis for the first and second cycling series, respectively. Additional strain broadening analysis beyond what is described in the Experimental Section is shown in Figure S9 (Supporting Information). During the first cycling series, in Figure 3, an increase in strain broadening is observed to correlate with the degree of lithiation, rising from 0.06 ± 0.03 (%) to a maximum value of 0.54 ± 0.05 (%) during the first lithiation cycle (see Table 1 for strain broadening coefficient fits). Additionally, the maximum broadening also occurs as the maximum lattice compressive strain is reached at the end of L1, indicating an uneven distribution of lithiation-induced strain in the scaffold. While the maximum broadening occurs as the maximum degree of lithiation, the minimum broadening is actually observed during the middle of lithiation and delithiation steps (marked with “Cell Potential” in Figure 4) corresponding with changes in the slope of the in-plane strain curve after the first lithiation, L1. The correlation between broadening minima and slope changes in the strain curve provides further evidence that the mechanism of deformation changes at these time points and may be the effects of accumulated and on-going inelastic deformation. Additionally, considering the evolution of broadening over the first cycling series, the maximum broadening observed at both the maximum and minimum lithiation states decreases from L1 to L2 to L3 and D1 to D2 to D3, respectively, further consistent with the accumulation of inelastic deformation (see Table 1 for strain broadening coefficient fits).

During the second cycling series in Figure 4, the strain broadening follows very similar behavior to that observed in the first series, even at a higher cycling rate. At much higher degrees of lithiation in L7, the broadening exceeds the highest value measured during the first cycling series, rising to a maximum of 0.71 ± 0.04 (%). The higher broadening, along with a larger in-plane average compressive strain of 1100 ± 200 $\mu\epsilon$, indicates that the degree of lithiation attained in the Si active layer during this cycle is likely higher than any previous lithiations of the Si. A higher degree of lithiation is expected in L7 given that the lower voltage cut-off during cycling was decreased to 10 from 100 mV in previous cycles, adding additional, previously unused capacity. In the high cycling rate region (D7, C8, and C9), the minima in broadening occur just after the beginning of (de)lithiation, indicative of a rapid surface (de)lithiation before the bulk of (de)lithiation progresses.

3. Discussion

3.1. In-Plane Average Lattice Strain Measurements

The inverse opal Ni scaffold can be conceptually simplified to be a network of nodes and struts, where the struts and nodes comprise 40% and 60%, respectively (40% cuboidal nodes and 20% tetrahedral nodes), of the volume of Ni in the scaffold, which comprises 26% of the total volume of the structure, while Si represents 24% (see Figure S11, Supporting Information, for assumptions and derivation). While 30 nm of Si evenly

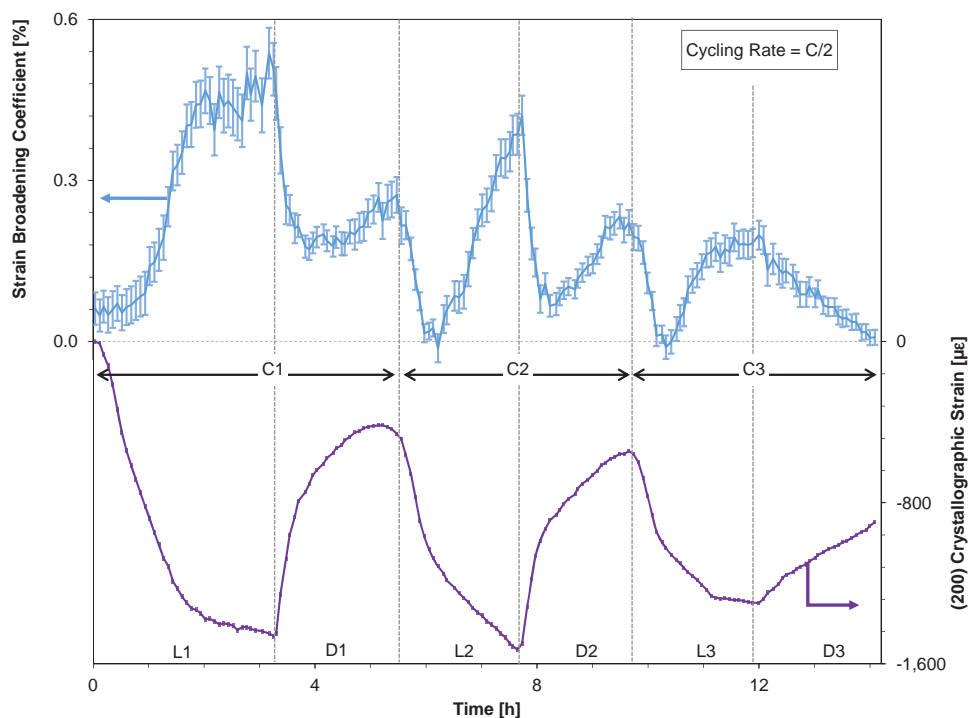


Figure 3. Time dependence of strain broadening coefficient as calculated for Ni (111), (200), and (220) (left axis) and in-plane average crystallographic strain (right axis, as in Figures 1 and 2) (Series 1 consisting of cycles C1, C2, and C3, where the lithiation and delithiation steps in C1 are denoted L1 and D1, respectively, and so on for C2 and C3). The error for the strain broadening coefficient is approximated as the norm of the residuals of fitting for each pattern and the error for the in-plane average strain is on the order of the line thickness of the curve.

coats both the nodes and struts, the Si coating on the struts may lithiate faster than the coating on the nodes due to the lower amount of Ni and thus reduced mechanical constraining stresses and a correspondingly higher diffusivity of Li in the struts. The higher compliance in the struts is due to the lower relative volume of Ni in the strut versus the node in comparison to the amount of Si coating the scaffold. Preferential (de)lithiation then could build a strain gradient between the nodes and struts, causing higher strains in the struts during lithiation than in the nodes, and broaden the elastic strain measured in the anode itself. This preferential (de)lithiation would also explain slope changes and nonlinearity in the average strain response of the scaffold during cycling, as preferential (de)lithiation will shift the average strain rate when (de)lithiation in the struts becomes more or less prevalent.

The strains created in the Ni scaffold during anode lithiation are compressive as expected from the Si expansion on lithiation. The reason compressive strains are observed in the Ni during Si lithiation-induced expansion is due to the diffusion-mediated process by which lithiation of the Si active layer occurs. During lithiation, Li⁺ ions are added into the Si active layer, inducing an expansion in the Si which occurs preferentially in unconstrained directions, in this case perpendicular to the Si free surface in contact with the solid electrolyte interphase (SEI) and electrolyte. While the Si active layer expands perpendicular to its free surface to ultimately nearly fill the pores in the inverse opal structure,^[34] expansion of Si towards the active layer scaffold interface is also expected to occur, but it is constrained by the Ni scaffold. The action of the Ni

scaffold to resist the expansion of the Si active layer thus puts the scaffold into net average compression, which increases as the degree of lithiation increases.

At the beginning of the lithiation step in any cycle (Figures 1 and 2), the slope of the Ni strain versus time curves are linear, but these slopes decrease with increasing lithiation. This behavior, along with the presence of plateaus in Ni strain at low voltages and high degrees of lithiation, indicate changes in the strain gradients in Si as the effects of stress–diffusion coupling become more pronounced (see Figures S6 and S7, Supporting Information, for the relationship between cell potential and capacity). Additionally, given that the stiffness and yield strength of a-Si decrease with increasing lithium concentration (with the yield strength of a-Si starting at 1 GPa^[13] and both stiffness and yield strength decreasing by ≈75% from pure a-Si to Li₁₅Si₄ (≈3580 mAh g⁻¹),^[10,35–37] plastic flow of the Si active layer during high degrees of lithiation may be occurring. The maximum specific capacity and thus degree of lithiation in this work is assumed to be 3100 mAh g⁻¹ for the first cycling series based on the work by Zhang and Braun^[34], where a similar inverse opal anode was cycled at a rate of 0.3C. Plastic flow in Si will reduce mismatch stresses with the Ni scaffold and thus keep the degree to which stress impedes Si-lithiation constant near the regions of Si which are plastically deforming. Plasticity in the Ni scaffold is also possible and will be discussed later. In addition to decreasing strain slopes and the presence of strain plateaus, plasticity in the Si may also contribute to the changes in the maximum Ni compressive stress measured at the maximum extent of lithiation.

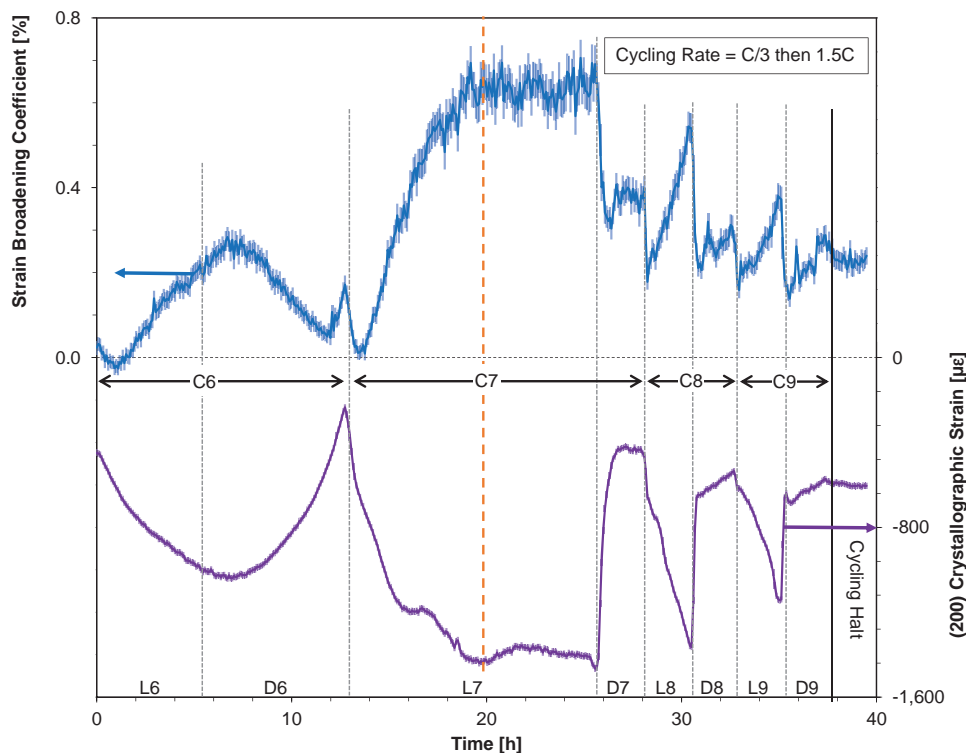


Figure 4. Time dependence of strain broadening coefficient as calculated for Ni (111), (200), and (220) (left axis) and in-plane average crystallographic strain (right axis, as in Figures 1 and 2) (Series 2 consisting of cycles C6, C7, C8, and C9, where the lithiation and delithiation steps in C6 are denoted L6 and D6, respectively, and so on for C7, C8, and C9). The error for the strain broadening coefficient is approximated as the norm of the residuals of fitting for each pattern and the error for the in-plane average strain is on the order of the line thickness of the curve. Lithiation at a potential < 100 mV starts at ~20 h (vertical orange dotted line).

Another explanation for a reduction in mismatch stress with the Ni scaffold from the Si active layer is the build-up of conductive delamination and damage. Given that the thickness of the Si coating is ≈ 30 nm, it is likely thinner than the critical crack size for lithiating a-Si (estimated to be on the order of 300 nm)^[38] and thus delamination is more likely than pulverization in this geometry.^[14,39,40] When a section of the Si coating delaminates while maintaining electrical contact with Ni scaffold, the resistance to electrical conduction through the a-Si may inhibit the overall rate of lithiation in the delaminated section relative to the intact active layer. This difference in lithiation rates causes the intact Si coating sections to lithiate and thus accumulates mismatch stresses more rapidly than the delaminated sections. Thus the overall lithiation process of the anode and accompanying lithiation-induced strains occur at two different rates: a faster rate when both the intact and delaminated sections lithiate and a slower rate (and thus lower mismatch strain rate) when only the partially delaminated section lithiates.

In addition to plasticity in the Si and delamination between the Ni and Si, plastic deformation in the Ni scaffold is also possible, as the maximum compressive stresses seen by the Ni scaffold during lithiation (up to 230 MPa), could approach or exceed the yield point of the Ni. Since these in operando diffraction measurements only measure strains (and indirectly stresses) in two dimensions, we are unable to directly quantify deviatoric stresses or evaluate von Mises stress and yield criteria. However, the high average values of compressive stresses

observed indicate that yielding could occur due to high deviatoric stresses in the Ni scaffold. Additionally, the X-ray beam averages strain in all three dimensions within the scaffold, as the beam passes through numerous scaffold layers that contain Ni crystallites oriented in many different directions. A flat thin film of electrodeposited Ni would be likely to have Ni crystallites with the (110) face normal to the substrate,^[41] but since the Ni was deposited onto 3D opals during fabrication, the average orientation of the crystallites is expected to be random.

Since the strains measured are normalized to the prelithiation strain state of the anode, the initial processing strains are unknown, as are the total strains on the system. During processing, thermal mismatch strains are expected to develop between the Ni scaffold, the Si substrate, and the a-Si active layer. The thermal expansion mismatch between the Si and Ni is expected to produce a tensile stress in the Ni on the order of 900 MPa,^[42,43] some of which will be accommodated by plasticity in the Ni or a-Si or by delamination upon cooling, as the yield stress of the Ni is expected to be on the order of 600 MPa.^[44] Therefore, residual tensile stresses from processing in the Ni would counteract lithiation-induced compressive stresses and thus increase the range of lithiation-induced strain that the scaffold is able to elastically accommodate prior to yielding. Additionally, given that the yield strength of a-Si decreases below the yield strength of the Ni upon increasing lithiation, plastic deformation is more likely to occur first in the lithiated a-Si than the Ni scaffold.

With plasticity possible in both the Ni and Si, and delamination possible between the two, high degrees of lithiation do not produce only one obvious deformation mechanism. At the extremes of the state of charge of the Si, elasto-plastic behavior in either the Si or the Ni, and/or damage and delamination could produce strain versus time/charge curves with decreasing slope due either to plastic deformation accommodating some of the (de)lithiation stress or a decrease in mismatch stress between the lithiating Si and the Ni scaffold. Strain broadening measurements provide a more detailed picture of strain inhomogeneity in the Ni elastic response, but 3D finite element modeling, which is beyond the scope of the present paper, will be necessary to fully describe the distribution of strains and the degree of plasticity, as well as the extent of damage and delamination observed in both the Ni and Si components. Separating the contributions of plasticity and damage could be achieved experimentally using advanced in operando microscopy techniques (such as TEM or advanced, fine resolution transmission X-ray microscopy) to directly observe conductive delamination between the Si and the Ni scaffold, or electrochemical impedance spectroscopy at various states of charge over multiple cycles to observe changes in the amount of free surface present and potential increases in resistance from delamination in the anode.

Examining the higher cycling rate regime (D7, C8, and C9 in Figure 2), it is apparent that both capacity and strain state are sensitive to the cycling rate. This cycling rate sensitivity confirms the known difficulty of fully lithiating an electrode given sluggish lithiation kinetics,^[9] especially when a high over-potential causes the cell operating voltage to approach 0 V relative to Li metal. Since a high degree of lithiation had been achieved prior to D7 and the beginning of rapid cycling, and the allowable over-potential window on delithiation was likely larger than on lithiation, it is also possible that the amount of lithium that was able to be extracted during delithiation was greater than the amount of lithium alloyed during subsequent relithiation. Therefore, the reversible lithiation capacity observed in D7, C8, and C9 may be higher than what would have been achieved had rapid cycling began with delithiated Si, as excess lithium would be able to be extracted each cycle. This is also supported by the high Coulombic efficiency in C8 and C9 (see Figure S8, Supporting Information). Thus it is possible that the lithiation step is kinetically slower or able to (de)alloy less lithium than the delithiation step for the same cycling rate and further studies will be required to explore the exact rate sensitivity of lithiation versus delithiation.

3.2. Lattice Strain Broadening Coefficient Analysis

Strain broadening analysis provides a more detailed picture of the state of strain present in the scaffold during (de)lithiation. The increase in strain broadening during lithiation, as seen in Figures 3 and 4, is likely due to the presence of strain gradients, the influence of the inverse opal structure on the mechanics of lithiation, plasticity in the Ni scaffold and/or Si active layer, and/or delamination between the Ni scaffold and Si active layer.

Strain broadening is positively correlated with the degree of lithiation in the anode material and related closely to the

measured average strain. Strain broadening minima were expected to be present at the lowest degrees of lithiation corresponding to minima in compressive strain, assuming a completely reversible lithiation process, but were instead observed at intermediate cell potentials and measured strain values between full lithiation and full delithiation (see Figures S6 and S7, Supporting Information, for the relationship between cell potential and capacity). These local broadening minima could confirm a preferential (de)lithiation of the struts over the nodes in the structure, which would explain why this behavior was observed at multiple cycling rates during the experiment.

Another explanation for these local broadening minima is that these charge states correspond to an exact balancing, within the scaffold, of lithiation-induced compressive strains and residual processing tensile strains. Once the Li concentration begins to change from maximum (during delithiation) or minimum (during lithiation), the Ni strains elastically; at a certain Li concentration, these compressive strains on average cancel out the residual tensile elastic strain state in the Ni, thereby minimizing the broadness of the distribution of total strain. As the concentration of lithium and lithiation-induced compressive strains change further, the average lattice spacing begins to deviate again from exactly matching the residual tensile strain state of the lattice, thus increasing the measured strain broadening. Finite element modeling will be necessary to fully understand to what extent inelastic deformation versus the geometry of the scaffold causes the presence of these minima in the strain broadening coefficient.

In addition to the broadening minima behavior, the decrease in the strain broadening maxima between cycles can be explained by plastic deformation and/or delamination and damage. As lithiation occurs, the lithiated Si could plastically flow in response to the stress state present in the anode assembly. This plastic flow would act to reduce any regions of stress concentration in the Ni at that stress state and thus prevent further increases in the overall distribution of strain measured in the Ni as the anode approaches the maximum degree of lithiation. Plastic deformation would also be expected to increase the minimum of the strain broadening coefficient by forming residual stresses and strains in and around plastically deforming grains. However, since ratcheting increases in the strain broadening minima are not observed in the data, delamination and damage are more likely responsible for the decrease in strain broadening maxima and inelastic deformation during cycling. During cycling, damaged Si regions of the anode could reach high strain states relative to undamaged regions, initially creating a wide distribution of strains measured in Ni. At high stresses, delamination in these regions that does not result in electrical isolation may occur, which would reduce the lithiation-induced mismatch stress with the scaffold in regions of previously high strain states and thus narrow the distribution of measured strains as cycling progresses. Finite element modeling will be necessary elucidate the competing contributions of plasticity, damage, and delamination phenomena on the decrease in maximum strain broadening values observed over several cycles.

Overall, Ni scaffold in operando XRD strain measurement is an indirect but sensitive method to measure the rate sensitivity of strain and capacity in battery electrodes. Using XRD-based

strain measurements, it is possible to measure both average strains and the distribution of strain within all of the diffracting phases present in a sample. As compared to in situ TEM, AFM or in operando substrate curvature measurements,^[8,10,11,13–17] in operando XRD-based strain measurements not only allow for larger, micro- or nanostructured, lab-scale samples to be probed while employing galvanostatic cycling conditions but also enables simultaneous phase composition and quantification analysis for samples that may undergo crystalline phase transitions. Thus in operando X-ray diffraction is a very powerful method for characterizing transient phenomena in battery materials.

4. Conclusion

The elastic strains in a nickel inverse opal scaffold coated with Si undergoing (de)lithiation were measured in operando, at different electrochemical cycling rates, using synchrotron-based X-ray diffraction. Quantitative strain measurements were collected for the Ni scaffold during cycling, resulting from mismatch stresses between the inactive Ni scaffold and the Si active material undergoing large volumetric changes during (de)lithiation. Compressive lattice strains measured in the Ni are consistent with the view that lithiating Si expands outward from surfaces and interfaces and that a mismatch stress between Si and the surrounding Ni scaffold builds during lithiation. The observed increase in Ni lattice strain broadening with increasing Si lithiation indicates that strains and stresses in the nanostructure are nonuniform, which is expected given the node and strut geometry of the inverse opal scaffold. The nonuniformity of the scaffold may also cause nonuniform (de)lithiation in the active layer, as indicated by the minima in the strain broadening.

Plasticity is expected to have measurable impact on cycling; plastic deformation in Ni and/or Si may be inferred from the change in the strain rate during (de)lithiation as well as the changes in fully lithiated and recovered strains. Damage and delamination of the Si from the Ni also has a measurable impact on cycling and mismatch stress behavior, which was inferred from a decrease in Ni strains and strain broadening maxima at full Si lithiation, as well as the appearance of two different strain rates during Si (de)lithiation. Additionally, (dis)charging rate sensitivity in both capacity and strain were observed to be correlated with each other during cycling even with a high initial lithiation state.

Employing a calculated crystallographic stress to relate the strains measured in the Ni to average Ni stresses, compressive strains of up to $1100 \pm 200 \mu\epsilon$ in Ni (311) correspond to average compressive stress of 230 ± 40 MPa. While this simple crystallographic stress approximation is sufficient to provide an estimate of the average stresses present in the scaffold, detailed finite element modeling will be needed to fully quantify the stress–strain distribution in both the Ni and Si and to describe the extent to which plastic deformation and interfacial damage influences the Ni elastic strain response.

Besides demonstrating that XRD-based strain measurement of the inactive Ni substrate is an indirect but sensitive method to follow strains in the active Si phase, our results suggest that in nanostructured anodes, inelastic deformation due to

lithiation-induced volume changes evolves from cycle to cycle, and that this deformation, which may lead to eventual mechanical failure, begins developing during the first few cycles of the anode.

5. Experimental Section

Electrode Preparation: The preparation of bicontinuous inverse opal silicon battery anodes is described in detail by Zhang and Braun^[34] and Zhang et al.^[45] Briefly, to prepare $\approx 10 \mu\text{m}$ thick opal nickel template structures, 500 nm diameter polystyrene (PS) spheres, are self-assembled on a gold-coated 500 μm thick single crystal silicon (100) substrate (coated with its native oxide). The PS sphere arrangement is then heated at a temperature near the glass-transition temperature of the PS to strengthen the opal template structure, after which Ni is electrodeposited into the void space of the PS opal template. The PS template is then removed with tetrahydrofuran, exposing a Ni inverse opal scaffold with narrow struts interconnected between spherical voids. The scaffold is then electrochemically etched to increase the window size between voids and the porosity of the structure. Finally, a thin (≈ 30 nm) film of amorphous Si is deposited onto the Ni scaffold through chemical vapor deposition at 400 °C using disilane as the Si source. A schematic of a fabricated inverse opal unit cell is shown in **Figure 5**.

Electrochemical Cell Fabrication: Electrochemical pouch cells were prepared to perform in operando diffraction measurements of the Si-coated Ni scaffold as shown in **Figure 5**. The Si anode was attached to an external nickel electrical contact via conductive carbon tape attached to the gold coating on the Si substrate. A Celgard 2500 polypropylene separator was placed between the anode and a 380 μm thick lithium counter electrode, with the whole assembly bathed in a nonaqueous electrolyte (1 M LiClO₄ dissolved into a 1:1 mixture of ethylene carbonate and dimethylene carbonate) and sealed in a polyamide-coated aluminum pouch inside of an argon-filled glove box.

In Operando X-Ray Diffraction Measurements: Diffraction experiments were performed at the Advanced Photon Source (APS), at Argonne National Laboratory, using the beam line station 1-BM-C. A monochromatic X-ray with an energy of 20.25 keV ($\lambda = 0.061234$ nm) and a 300 μm beam diameter shined on the center of the sample, aligned such that all elements of the electrochemical pouch cell, including the Ni scaffold, Si substrate, Li counter electrode, and aluminum pouch walls were nearly normal to the beam direction, as shown in **Figure 5**. Diffraction patterns were recorded in a transmission geometry and taken every 5 min with a 30 s exposure time with an a-Si PerkinElmer 2048 × 2048 pixel area detector with a 200 μm × 200 μm pixel size and a 16-bit dynamic range placed at 396 mm from the sample. The sample was slightly tilted to ensure the single crystal Si substrate peaks were out of the Bragg condition to reduce any strong diffraction spots onto the detector. A diffraction pattern from a reference powder sample of LaB₆ (1 mm kapton capillary tube filled with National Institute of Standards and Technology (NIST) Standard Reference Material 660b) and the software FIT2D^[46] was used to determine the center of the diffraction patterns, to correct for detector tilts relative to the sample and the beam, to determine the sample-to-detector distance and to provide a calibration standard for the instrumental and geometric peak widths. The electrochemical cell cycling parameters are described in the Supporting Information.

Fitting of Diffraction Peaks: Diffraction rings from the nickel inverse opal scaffold were fit to determine the lattice strains present in the scaffold during electrochemical cycling. The intensity of nickel diffraction rings were nearly continuous with azimuth, with some variation attributed to the small volume ($\approx 7 \times 10^5 \mu\text{m}^3$) of the nickel scaffold and limited averaging associated with fitting. No distinct scattering signal from the a-Si active material was observed, and scattering signals from the Al pouch and Si substrate, though present, were not fit given that these phases did not contribute to the electrochemical performance of the cell. The diffraction peaks for selected reflections (Ni (111), Ni

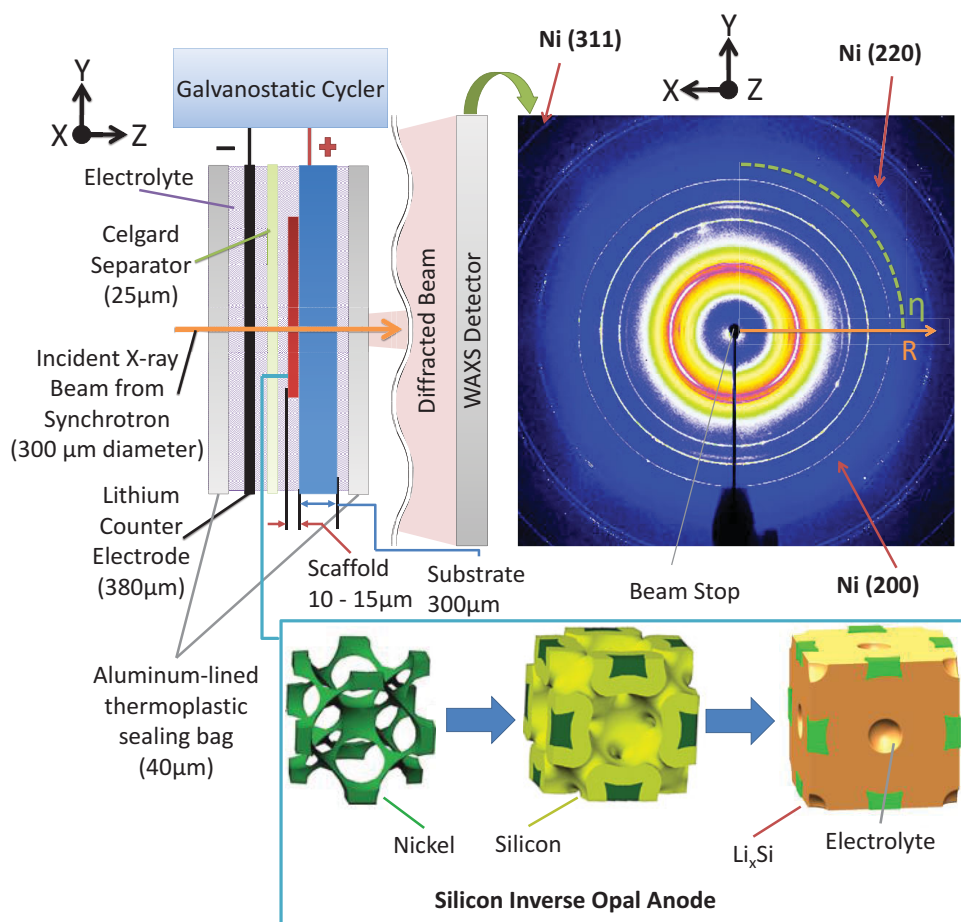


Figure 5. Schematic of in operando X-ray diffraction measurements including a cell schematic (left), a representative diffraction pattern extracted from diffraction data in the first lithiation L1 (right), and a bicontinuous silicon inverse opal anode unit cell, showing the Ni scaffold alone (bottom left), the scaffold coated with a-Si (bottom middle), and the lithiated structure (bottom right). Electrolyte is not shown, and channels, not shown in the schematic, for Li-ion transport remain open on the lithiated structure. Figures bottom left and bottom middle are adapted with permission.^[34] Copyright 2012, American Chemical Society.

(200), Ni (220), and Ni (311)) were fit to pseudo-Voigt profiles, and the resultant peak positions as a function of azimuth were used to compute lattice strains.^[19–23,26,47] The fitting algorithm is implemented in a series of MATLAB programs developed at the APS, with additional details included in the Supporting Information. In addition to peak position, the full width half maximum (FWHM) from the pseudo-Voigt fits was also used to quantify the breadth of each peak.

Determination of In-Plane Average Lattice Strain: After calibrating the detector, the lattice spacings for the Ni (111), Ni (200), Ni (220), and Ni (311) diffraction rings were calculated and the relative strain was determined by

$$\varepsilon_{\text{avg}} = \frac{d_{(hkl)} - d_{(hkl)}^0}{d_{(hkl)}^0} \quad (1)$$

where ε_{avg} refers to the average relative strain measured over the selected azimuthal sections of the diffraction pattern. Here, $d_{(hkl)}^0$ refers to lattice spacing for the first diffraction pattern collected during the experiment, before any appreciable lithiation of the anode has occurred. No systematic invariant points in measured $d_{(hkl)}$ as a function of azimuth (η) were observed in any of the Ni diffraction rings, thus precluding the examination of principal strains or pure deviatoric strains. The error in the calculated ε_{avg} was approximated as the average in quadrature of the errors in fitting each respective diffraction ring in the selected azimuthal sections.

The averaged strain over the full powder ring (averaged over 350° due to the X-ray beam stop support blocking 10°) represents the average of the strain in two dimensions and is termed the in-plane average strain, as the third dimension is perpendicular to the plane where the Bragg condition is satisfied for all of the measured diffraction rings.

Determination of the Lattice Strain Broadening Coefficient: Based on the work of Williamson and Hall,^[48] it is possible to not only fit the average ring position but also describe the distribution of strain across a crystal using the modified Scherrer equation, using each diffraction ring's FWHM and scattering angle. The strain broadening coefficient can be calculated by fitting

$$\beta \cos(\theta) = \frac{k\lambda}{D} + \xi \sin(\theta) \quad (2)$$

to all of the available diffraction rings in one phase using a least-squares linear regression, where β is the sample peak FWHM, θ is the scattering angle of that diffraction peak, k is the shape factor (in this work assumed to be unity for low aspect ratio crystallites), λ is the incident X-ray wavelength, D is the average crystallite size, and ξ is the desired strain broadening coefficient. A representative plot and fit for a single diffraction pattern is shown in Figure S10 (Supporting Information).

The LaB₆ calibration standard was used in order to subtract instrumental and geometric contributions to the FWHM from the total measured Ni FWHM. The LaB₆ was assumed to have a negligible sample contribution so that the measured FWHM represents the instrumental

contribution. The measured LaB_6 FWHM was fit using a least squares linear regression as a function of $\sin(\theta)$ and this function was then subtracted from the Ni FWHM using the following equation:

$$\text{FWHM}_{\text{Ni}} = \sqrt{\text{FWHM}_{\text{Meas}}^2 - (A \sin(\theta) + B)^2} \quad (3)$$

where the second term in the square root is the LaB_6 -based correction with $A = 3.1639$ and $B = 2.3415$. Using the corrected Ni sample FWHM and the modified Scherrer equation, the strain broadening coefficient ξ was fit for all of the measured diffraction patterns using the Ni (111), (200), and (220) peaks. The error in fitting ξ was approximated as the norm of the residuals from fitting. The incompleteness of the Ni (311) diffraction ring precluded robust measurements of its FWHM, so this peak was excluded from the fitting of the strain broadening coefficient.

Supporting Information

Supporting Information is available from the Wiley Online Library or from the author.

Acknowledgements

This research was supported by the U.S. Department of Energy, Office of Science, Office of Basic Energy Sciences, under Contract No. DE-AC02-06CH11357 (electrochemical and X-ray characterization) and DE-FG02-07ER46471 (electrode fabrication). The authors thank Z. Liu, C. Hayner, and D. Snyder (Northwestern University) for their helpful discussions and assistance during data collection and analysis, J. Wang (University of Illinois at Urbana-Champaign) for assistance throughout the project, and the staff of Sector 1 of the Advanced Photon Source (Argonne National Laboratory) for assistance in experiments and data acquisition. Use of the Advanced Photon Source, an Office of Science User Facility operated for the U.S. Department of Energy (DOE) Office of Science by Argonne National Laboratory, was supported by the U.S. DOE under Contract No. DE-AC02-06CH11357.

Received: March 5, 2015

Revised: April 16, 2015

Published online: May 26, 2015

- [1] J. M. Tarascon, M. Armand, *Nature* **2001**, 414, 359.
- [2] R. Marom, S. F. Amalraj, N. Leifer, D. Jacob, D. Aurbach, *J. Mater. Chem.* **2011**, 21, 9938.
- [3] M. S. Whittingham, *Proc. IEEE* **2012**, 100, 1518.
- [4] M.-K. Song, S. Park, F. M. Alamgir, J. Cho, M. Liu, *Mater. Sci. Eng., R-Rep.* **2011**, 72, 203.
- [5] M. N. Obrovac, L. Christensen, *Electrochem. Solid-State Lett.* **2004**, 7, A93.
- [6] W.-J. Zhang, *J. Power Sources* **2011**, 196, 13.
- [7] C. M. Hayner, X. Zhao, H. H. Kung, *Annu. Rev. Chem. Biomol. Eng.* **2012**, 3, 445.
- [8] A. Mukhopadhyay, B. W. Sheldon, *Prog. Mater. Sci.* **2014**, 63, 58.
- [9] M. T. McDowell, S. W. Lee, W. D. Nix, Y. Cui, *Adv. Mater.* **2013**, 25, 4966.
- [10] M. T. McDowell, I. Ryu, S. W. Lee, C. Wang, W. D. Nix, Y. Cui, *Adv. Mater.* **2012**, 24, 6034.
- [11] L. Y. Beaulieu, T. D. Hatchard, A. Bonakdarpour, M. D. Fleischauer, J. R. Dahn, *J. Electrochem. Soc.* **2003**, 150, A1457.
- [12] V. A. Sethuraman, M. J. Chon, M. Shimshak, N. Van Winkle, P. R. Guduru, *Electrochem. Commun.* **2010**, 12, 1614.
- [13] V. A. Sethuraman, M. J. Chon, M. Shimshak, V. Srinivasan, P. R. Guduru, *J. Power Sources* **2010**, 195, 5062.
- [14] J. W. Wang, X.-H. Liu, K. Zhao, A. Palmer, E. Patten, D. Burton, S. X. Mao, Z. Suo, J. Y. Huang, *ACS Nano* **2012**, 6, 9158.
- [15] M. Gu, Y. Li, X. Li, S. Hu, X. Zhang, W. Xu, S. Thevuthasan, D. R. Baer, J.-G. Zhang, J. Liu, C. Wang, *ACS Nano* **2012**, 6, 8439.
- [16] C. R. Becker, K. E. Strawhecker, Q. P. McAllister, C. A. Lundgren, *ACS Nano* **2013**, 7, 9173.
- [17] S.-J. Lee, J.-K. Lee, S.-H. Chung, H.-Y. Lee, S.-M. Lee, H.-K. Baik, *J. Power Sources* **2001**, 97–98, 191.
- [18] M. T. McDowell, S. W. Lee, C. Wang, Y. Cui, *Nano Energy* **2012**, 1, 401.
- [19] A. Wanner, D. C. Dunand, *Metall. Mater. Trans. A* **2000**, 31, 2949.
- [20] M. L. Young, J. DeFouw, J. D. Almer, D. C. Dunand, *Acta Mater.* **2007**, 55, 3467.
- [21] J. D. Almer, S. R. Stock, *J. Struct. Biol.* **2005**, 152, 14.
- [22] C. Weyant, J. D. Almer, K. Faber, *Acta Mater.* **2010**, 58, 943.
- [23] M. R. Daymond, M. L. Young, J. D. Almer, D. C. Dunand, *Acta Mater.* **2007**, 55, 3929.
- [24] N. S. Rossini, M. Dassisti, K. Y. Benyounis, A. G. Olabi, *Mater. Des.* **2012**, 35, 572.
- [25] I. C. Noyan, T. C. Huang, B. R. York, *Crit. Rev. Solid State Mater. Sci.* **1995**, 20, 125.
- [26] A. C. Deymier-Black, J. D. Almer, S. R. Stock, D. R. Haeffner, D. C. Dunand, *Acta Biomater.* **2010**, 6, 2172.
- [27] D. K. Balch, E. Üstündag, D. C. Dunand, *Metall. Mater. Trans. A* **2003**, 34, 1787.
- [28] F. Wang, L. Wu, B. Key, X.-Q. Yang, C. P. Grey, Y. Zhu, J. Graetz, *Adv. Energy Mater.* **2013**, 3, 1324.
- [29] T. D. Hatchard, J. R. Dahn, *J. Electrochem. Soc.* **2004**, 151, A838.
- [30] J. Li, J. R. Dahn, *J. Electrochem. Soc.* **2007**, 154, 156.
- [31] S. Misra, N. Liu, J. Nelson, S. S. Hong, Y. Cui, M. F. Toney, *ACS Nano* **2012**, 6, 5465.
- [32] X.-Q. Yang, J. McBreen, W.-S. Yoon, M. Yoshio, H. Wang, K. Fukuda, T. Umeno, *Electrochem. Commun.* **2002**, 4, 893.
- [33] T. H. Courtney, *Mechanical Behavior of Materials*, Waveland Press, Inc., Long Grove, IL **2000**.
- [34] H. Zhang, P. V Braun, *Nano Lett.* **2012**, 12, 2778.
- [35] B. Hertzberg, J. Benson, G. Yushin, *Electrochem. Commun.* **2011**, 13, 818.
- [36] A. Kushima, J. Y. Huang, J. Li, *ACS Nano* **2012**, 6, 9425.
- [37] J. Moon, K. Cho, M. Cho, *Int. J. Precis. Eng. Manuf.* **2012**, 13, 1191.
- [38] I. Ryu, J. W. Choi, Y. Cui, W. D. Nix, *J. Mech. Phys. Solids* **2011**, 59, 1717.
- [39] T. K. Bhandakkar, H. Gao, *Int. J. Solids Struct.* **2010**, 47, 1424.
- [40] I. Ryu, J. W. Choi, Y. Cui, W. D. Nix, *J. Mech. Phys. Solids* **2011**, 59, 1717.
- [41] C. Kollia, N. Spyrellis, *Surf. Coatings Technol.* **1993**, 57, 1.
- [42] J. Fabian, P. Allen, *Phys. Rev. Lett.* **1997**, 1885.
- [43] *Handbook of Chemistry and Physics* (Eds: W. M. Haynes, T. J. Bruno, D. R. Lide) CRC Press Inc, Boca Raton, FL **2014**.
- [44] F. Ebrahimi, G. Bourne, M. Kelly, T. Matthews, *Nanostruct. Mater.* **1999**, 11, 343.
- [45] H. Zhang, X. Yu, P. V Braun, *Nat. Nanotechnol.* **2011**, 6, 277.
- [46] A. P. Hammersley, S. O. Svensson, A. Thompson, H. Graafsma, A. Kwick, J. P. Moy, *Rev. Sci. Instrum.* **1995**, 66, 2729.
- [47] B. J. Harder, J. D. Almer, C. M. Weyant, K. N. Lee, K. T. Faber, *J. Am. Ceram. Soc.* **2009**, 92, 452.
- [48] G. K. Williamson, W. H. Hall, *Acta Metall.* **1953**, 1, 22.